Journal of Electroanalytical Chemistry 984 (2025) 119054

Contents lists available at ScienceDirect

Journal of Electroanalytical Chemistry

journal homepage: www.elsevier.com/locate/jelechem

Carbon-based thick films for electrochemical detection of neonicotinoid insecticides

Barbara Repič [a,b], Gregor Marolt [c], Danjela Kuscer [a,b,*]

[a] Jožef Stefan Institute, Electronic Ceramics Department, Jamova cesta 39, Ljubljana, Slovenia
[b] Jožef Stefan International Postgraduate School, Jamova cesta 39, Ljubljana, Slovenia
[c] University of Ljubljana, Faculty of Chemistry and Chemical Technology, Večna pot, 113, Ljubljana, Slovenia

ARTICLE INFO

Keywords:
Graphite
Glassy carbon
Carbon black
Screen-printed electrode
Electrochemistry
Neonicotinoids

ABSTRACT

Neonicotinoids (NNIs) are water-soluble, toxic, widespread-used systemic insecticides commonly found in the environment. Integrated electrochemical sensors enable the rapid on-site detection of NNIs in aqueous samples by analysing the reduction of the NNI's nitro functional group on the working electrode. We have investigated graphite (G), glassy carbon (GC) and carbon black (CB) thick films as working electrodes for the electrochemical detection of the NNI imidacloprid (IMD). Up to 35-μm-thick films of G, GC and CB on alumina were prepared by screen printing and subsequent firing at 850 °C in argon. G had the largest grain size, the roughest surface, and the lowest sheet resistance of 6.9 Ω/sq. GC and CB had a smoother surface, while their sheet resistances were up to 27 Ω/sq. All three films showed a reversible response to the $Fe(CN)_6^{3-/4-}$ redox probe with G having the highest electrochemically active surface area and the highest heterogeneous electron transfer rate constant. In the IMD solution with neutral pH, G, GC and CB exhibited characteristic reduction peak at −1.1 V and a re-oxidation peak at +0.2 V. An additional adsorption cathodic peak was observed with CB, indicating a significantly higher affinity of CB for IMD adsorption. With LODs under 1 μM, the G, GC and CB pristine thick films exhibiting great potential for the sensitive detection of IMD.

1. Introduction

Neonicotinoids (NNIs) are systemic insecticides that are effective against a broad spectrum of crop pests and are therefore used in agriculture on a mass scale and frequently with a lack of restraint. NNIs with -N-NO_2 group, including imidacloprid (IMD), thiamethoxam (THX), and clothianidin (CLO), are toxic to pollinators and aquatic invertebrates. They accumulate in the soil and leach easily into water sources. As they are very persistent, their harmful effects are long-lasting [1–3]. Thus, rapid on-site determination of NNIs is required. NNIs with -NO_2 group can be directly detected by electrochemical (EC) methods exploiting irreversible reduction of -NO_2 on the electrode surface at negative potential. On mercury-based electrodes two reduction signals are observed, namely i) a four-electron reduction of the nitro group to the hydroxylamine derivative and ii) a further two-electron reduction of the hydroxylamine to the amine. The intensity of this second signal is half that of the first, as expected considering the number of exchanged electrons. Both cathodic processes are strongly dependent on pH, since protons are involved in the reduction reactions. A neutral or slightly alkaline pH of 7–10 is most suitable for the detection of these NNIs [4–6]. The main challenge in electrochemical detection of NNIs is to ensure that both the working electrode (WE) and the electrolyte remain stable in a fairly negative potential range, typically from −0.8 V to −1.6 V vs Ag/AgCl, where the reduction of NNI is expected to occur [5]. Therefore, the selection of the appropriate potential window for a given WE and supporting electrolyte is important as well.

Various WE materials have been investigated for the detection of NNIs. While the use of mercury-based WE has been avoided due to the toxicity of Hg [4–6], alternatives such as amalgam, metal-based material, metal-organic frameworks and carbon-based WE have been reported [7–10]. Among them, carbon-based materials are characterised by high specific surface area, high electrical conductivity, availability and low cost, making them one of the most widely used electrode materials. The reduction of the nitro group on the widely used glassy carbon disc electrode (GCE) proceeds differently than on the mercury-based electrode. Usually one reduction peak is observed in a cyclic voltammogram, which corresponds to the reduction of the -NO_2 group to hydroxylamine via a slow one-electron and a fast three-electron transfer

* Corresponding author at: Jožef Stefan Institute, Electronic Ceramics Department, Jamova cesta 39, Ljubljana, Slovenia.
E-mail address: danjela.kuscer@ijs.si (D. Kuscer).

https://doi.org/10.1016/j.jelechem.2025.119054
Received 5 December 2024; Received in revised form 13 February 2025; Accepted 25 February 2025
Available online 26 February 2025

process as shown in Fig. 1 [11,12]. To improve the sensitivity and selectivity of the WE, the electrode surface is commonly modified with various materials such as metals, metal oxides, carbon-based nanomaterials, supramolecular hosts, molecularly imprinted polymers or biorecognition agents such as enzymes, antibodies, aptamers and quench bodies [13,14].

For the on-site detection of analytes electrochemical sensors should be small, portable and robust and thick film technology is commonly employed for their fabrication. The components of the sensors are integrated on a mechanically, temperature and chemically stable ceramic substrate, aluminium oxide, usually by screen printing and subsequent curing [15–18]. The electrical connections, counter and reference electrodes are commonly made from commercially available metal pastes that are fired in air at a temperature of up to 1200 °C. However, the processing of C-based WE in the form of thick film on alumina is challenging. It requires precise control of the chemical composition and rheological properties of the paste as well as the deposition process to ensure a uniform thickness of the layer. The post-deposition treatment is demanding due to different thermal expansion coefficients of the two materials which can lead to delamination or formation of cracks in the deposit during thermal treatment. In addition, the thermal treatment should be carried out in an oxygen-free environment at high temperatures to prevent the layer from decomposing and to achieve high electrical conductivity [19]. Graphite thick films are commonly made from commercially available pastes according to the procedures recommended by the supplier [20]. Thick films of other carbon-based materials such as carbon black, glassy carbon or nanostructured materials are rarely reported and little information has been provided on the formulation of the screen-printing paste and the curing process after deposition [21–25]. Thus, it is not surprising that the majority of integrated sensors are based on the commercially available carbon-based WE [20], which is further modified with other carbon-based materials such as carbon black, graphene, carbon nanotubes, and nanofibers [10,26,27]. These nanostructured materials improve analytical performance due to their large surface area, higher electrical conductivity, electrocatalytic activity, and adsorption capability [28,29]. However, the physicochemical properties of carbon electrodes strongly depend on the type of material, its hybridization state, structure, fabrication process and pretreatment of the electrode [27,30].

This paper investigates the development of thick films of graphite (G), glassy carbon (GC) and carbon black (CB) integrated onto an alumina substrate for the detection of imidacloprid (IMD). We processed these films with a self-developed paste that was screen-printed onto the alumina and then fired under controlled temperature and atmosphere conditions. All thick films exhibited a uniform surface, low sheet resistance, a large electrochemically active surface and a high rate of heterogeneous electron transfer. Our results show that the pristine G, GC and CB thick films can effectively detect IMD in aqueous samples without the need to modify or functionalise the electrode materials, reaching detection limits in the micromolar range. The innovation of this research lies in the effective processing of integrated thick films of GC and CB, materials that are not commonly used for screen-printed electrodes. Furthermore, these unmodified materials are shown to be capable of detecting IMD, opening the possibility for further use in miniature integrated electrochemical sensors.

2. Materials and methods

Thick films were prepared from graphite (graphite flake, 99.8 %, Alfa Aesar, Karlsruhe, Germany), glassy carbon (spherical powder, Thermo Fisher, Kandel, Germany) and furnace carbon black (special black 250, Evonik Carbon Black, Frankfurt, Germany) powders. Screen-printing pastes were prepared by dispersing 15 vol% of the powders in an organic vehicle, comprising α-terpineol (TPN, ≥98 %, Merck, Darmstadt, Germany), ethyl cellulose (EC, 48 % ethoxyl basis, Sigma Aldrich, St. Louis, MO, USA), and [2 − (2 − butoxyetoxy)ethyl] acetate (BEEA, ≥98 %, Merck, Darmstadt, Germany). The pastes were homogenised on a three-roll mill (Exact Technologies, Oklahoma City, OK, USA).

The self-developed carbon pastes were screen printed in 8 mm × 8 mm square-shaped patterns on an alumina substrate (96 % Al_2O_3, Rubalit 708S, CeramTec) using a screen printer (P-250AVF, KEKO Equipment, Žužemberk, Slovenia) as shown in Fig. 2a. Layers were dried at 120 °C for 15 min in air and subsequently fired in a tube furnace under argon flow. The layers were heated to 450 °C for 1 h at a heating rate of 2 °C min^{-1}, then further heated to 850 °C for 30 min at 5 °C min^{-1} and finally cooled to room temperature at a cooling rate of 5 °C min^{-1} [19]. The electrical connections were made from a colloidal silver paste (Ted Pella Inc., Redding, California, US). After screen printing, the silver paste was air dried at room temperature (Fig. 2b) and subsequently covered with a nitrocellulose-based dielectric layer, which was also air dried at room temperature (Fig. 2c).

All reagents for electrochemical measurements were of analytical grades and were used without further purification: sodium dihydrogen phosphate anhydrous (NaH_2PO_4, ≥99.0 %, Merck, Darmstadt, Germany), disodium hydrogen phosphate anhydrous (Na_2HPO_4, >99.0 %, Merck, Darmstadt, Germany), potassium hexacyanoferrate (II) trihydrate ($K_4[Fe(CN)_6]•3H_2O$, ≥98.5 %, Carlo Erba, Val-de-Reuil, France), potassium hexacyanoferrate (III) anhydrous ($K_3[Fe(CN)_6]$, ≥99 % Carlo Erba, Val-de-Reuil, France), hydrochloric acid (HCl, 37 %, Appli Chem, Dermstadt, Germany), sodium hydroxide (NaOH, ≥99.0 %, Merck, Darmstadt, Germany) and imidacloprid (IMD, $C_9H_{10}ClN_5O_2$, ≥98.0 %, Sigma Aldrich, Saint Louis, MO, USA). All solutions were prepared with ultrapure water (resistivity ≥18 MΩcm). The supporting electrolyte was a 0.1 M phosphate buffer solution (PBS) with a pH of 7.0, which was prepared by dissolving adequate amounts of NaH_2PO_4 and Na_2HPO_4 in ultrapure water. The pH of the solutions was adjusted using 1 M HCl or 1 M NaOH solution and measured with a pH meter (Mettler Toledo, Columbus, Ohio, USA). The redox probe used to evaluate the electrochemical response of the WEs was a 5 mM hexacyanoferrate (II)/(III) solution (HCF) with equimolar concentration of Fe^{2+}/Fe^{3+} in PBS. The voltametric response to IMD was investigated in a 1000 µM IMD solution in PBS. For the calibration curve, this solution was further diluted with PBS to obtain 100 µM, 10 µM and 1 µM IMD solutions in PBS. Before each voltammetric experiment, 50 mL of the solution in the

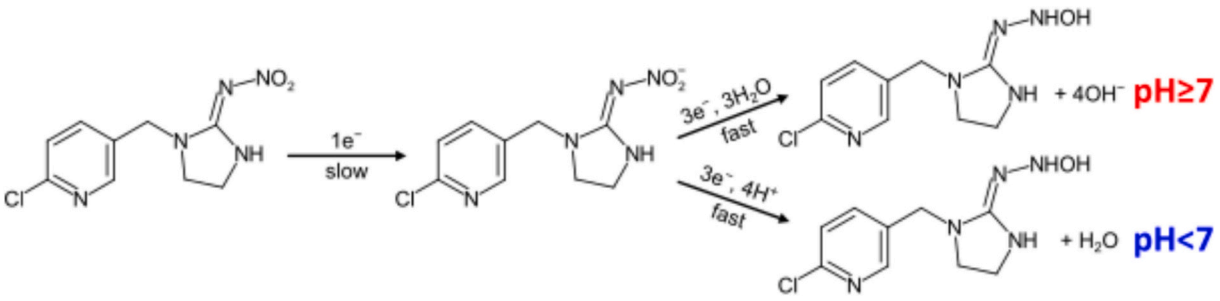

Fig. 1. Scheme of imidacloprid reduction on carbon working electrode in neutral or alkaline and acidic medium.

Fig. 2. Scheme of preparation of carbon WE with silver contacts covered with dielectric layer.

electrochemical cell was purged with nitrogen for 5 min.

The particle size and the particle size distribution of the powders were measured in isopropanol using a laser diffraction particle size analyser (S3500, Microtrac, York, PA, USA). All results were derived from the volume particle size distributions.

The X-ray powder diffraction (XRD) of the powders were collected at room temperature with a high-resolution diffractometer (X'Pert PRO MPD, PANalytical, Almelo, The Netherlands) using Cu $K\alpha_1$ radiation (λ = 1.5406 Å) in the reflection geometry. The diffraction patterns were collected in the 2θ range from 20° to 60° with a step of 0.034° and an integration time of 100 s per step. The phases were identified using X'Pert HighScore Plus 3.0e (PANalytical) and the PDF-4+/Web 2022 database.

The morphology of the powder and the surface of the films were investigated using a scanning electron microscope (SEM, Quanta 650 ESEM, Thermo Fisher Scientific, USA). The samples were analysed at an acceleration voltage of 15 kV.

The thermogravimetric analysis (TGA) of the carbon pastes was performed using a simultaneous thermal analyser (STA, 449 F3 Jupiter, Netzsch, LCC, Burlington, USA). About 40 mg of the paste was put in Al_2O_3 crucibles and analysed upon heating from 30 °C to 1200 °C at a heating rate of 2 °C min^{-1} in argon (5.0) with a flow rate of 100 mL min^{-1}.

The thickness of the prepared film was evaluated using a contact stylus profilometer (DektakXT Advanced System, Bruker, Billerica, MA, USA). The line profiles of the samples were measured at a scanning speed of 100 μm s^{-1} (resolution 0.33 μm pt^{-1}) using a stylus tip with 2 μm radius and 3 mg force. After levelling the data with a cubic curvature removal, the thickness of the layer t was determined as the average step height (ASH) of the film using the software Vision 64 (Bruker, USA). The root-mean-square surface roughness R_q was determined from the 6.5 mm roughness profile obtained after high-pass filtering of the primary profile using a Gaussian regression with a cut-off wavelength of 0.8 mm. The topography of the films was also analysed by atomic force microscopy (AFM, Jupiter XR, Asylum Research, Oxford Instruments, Santa Barbara, CA, USA). A silicon AFM tip (OMCL-AC200TS-R3, Olympus, Japan) was used to scan 80 μm × 80 μm areas in AC topography mode. The root-mean-square surface roughness R_q^{AFM} was calculated from the obtained AFM map scans.

The sheet resistance R_s of the films was determined by four-point probe technique using a high voltage source-measure unit (SMU, Keithley 237, Cleveland, Ohio, USA). We used a geometric correction factor of 0.795 for the calculation of R_s [19].

The electrochemical experiments were carried out using a potentiostat/galvanostat (Multi Autolab M 204, Methrom, The Netherlands) operated with Nova 2.1.5 software. Measurements were performed at 25 ± 0.5 °C in a 50 mL conventional three-electrode cell consisting of a commercially available Ag/AgCl (3.0 M KCl) reference electrode (RE), and a platinum sheet counter electrode (CE), both from Methrom, while the carbon-based thick films served as the working electrode (WE). Before recording the cyclic voltammograms (CVs), the open current potential (OCP) was measured. All CVs were recorded without ohmic drop compensation, first in a blank PBS and then in either HCF or IMD solution.

The CVs in HCF and corresponding PBS measurements on selected WEs were recorded between −0.2 V and +0.6 V from the initial potential of 0.0 V in the positive direction with a step potential of 2.44 mV at scan rates of 50, 100, 200, and 500 mV s^{-1}. The first set of measurements were performed in PBS by conducting 5 cycles at 100 mV s^{-1} to determine the capacitive current i_{cap} as the difference between cathodic and anodic current at +0.2 V. The reported value is an average value ($N = 5$) of i_{cap} determined for each cycle. The second set of measurements in PBS was performed by recording 3 cycles at all 4 given scan rates. This was followed by the measurements in HCF under the same conditions as in PBS. From these measurements, we determined the peak potential E_p and the peak current i_p as the difference between the current measured in HCF and the current measured in PBS (blank solution) at E_p. These values were used to calculate the ratio of cathodic to anodic peak current i_{pc}/i_{pa}, the peak to background (P/B) current ratio as the average ratio between i_{pc} or i_{pa} and the current measured in PBS (blank solution) at corresponding E_p, the peak-to-peak potential separation ΔE_p as the difference between the anodic (E_{pa}) and cathodic peak potentials (E_{pc}), and the half-wave potential $E_{1/2}$ as the mean value between E_{pa} and E_{pc}. The reported values are average values ($N = 5$) of the parameters determined for each cycle. From the CVs recorded in HCF at different scan rates, the electrochemically active surface area (A_{ecsa}) and the standard heterogeneous electron transfer rate constant (k^0) were determined.

A_{ecsa} has been calculated using the modified Randles-Ševčík equation for a quasi-reversible one-electron transfer process (Eq. (1)) [31],

$$i_p = 0.466 \bullet K(\Lambda, \alpha) \bullet n \bullet F \bullet A_{ecsa} \bullet C^0 \bullet \left(\frac{n \bullet F \bullet \nu \bullet D}{R \bullet T}\right)^{1/2} \quad (1)$$

where n is the number of electrons, F is the Faraday constant (96485 C mol^{-1}), C^0 is the molar concentration of the redox-active species, ν is the scan rate, D is the diffusion coefficient, R is the universal gas constant (8.314 J mol^{-1} K^{-1}), T is the temperature and $K(\Lambda,\alpha)$ is a modified dimensionless parameter for quasi-reversible reactions introduced by Matsuda et al (1955) [32]. To determine the parameter $K(\Lambda,\alpha)$, the dimensionless parameters $\Delta(\Lambda,\alpha)$ and Λ must first be calculated. The parameter $\Delta(\Lambda,\alpha)$ was calculated using the following equation: $\Delta(\Lambda, \alpha) = \left(E_{p/2} - E_p\right) / \left(\frac{RT}{F}\right)$, where $E_{p/2}$ is the peak potential at half peak current, and the parameter Λ was calculated using the following equation: $\Lambda = \Psi \sqrt{\pi}$, where π is the mathematical constant (3.14) and Ψ is a dimensionless kinetic parameter. The parameter Ψ acts as a polynomial function of the product $n\Delta E_p$ in the range 63 mV < $n\Delta E_p$ < 212 mV and was calculated using the empirical equation: $\Psi = \frac{(-0.6288 + 0.0021 \bullet n \bullet \Delta E_p)}{(1 - 0.017 \bullet n \bullet \Delta E_p)}$, which was developed by Lavagnini et al [33] from the experimentally determined ΔE_p and a known number of exchanged electrons during the redox process (one for HCF). The parameters $\Delta(\Lambda, \alpha)$ and Λ were calculated for the data obtained from the measured CVs at different ν. The electron transfer coefficient (α) was estimated geometrically from the plot $\Delta(\Lambda,\alpha)$ vs. log(Λ) (Fig. S3a) and the parameter $K(\Lambda,\alpha)$ from the plot $K(\Lambda,\alpha)$ vs. log(Λ) (Fig. S3b) [31]. The E_p, $E_{p/2}$ and ΔE_p values measured at different ν for G, GC and CB are listed in Table S1 in the Supporting information. Finally, A_{ecsa} was determined from the slope of the anodic peak currents (i_{pa}) vs. the square root of the scan rates ($\nu^{1/2}$), considering the diffusion coefficient of the oxidised, i.e. hexacyanoferrate(III) species, $D_O = 7.26 \bullet 10^{-6}$ cm^2 s^{-1} [34] and $K(\Lambda,\alpha)$ calculated for CV scans at 100 mV s^{-1}. The peak current density, j_p, was calculated by normalising i_p with A_{ecsa}.

The value of k^0 for scan rates at which the product $n\Delta E_p$ is between 63 mV and 212 mV was determined using the Nicholson method (Eq. (2)) [35,36], in which k^0 for a quasi-reversible electrochemical reactions is related to a dimensionless kinetic parameter Ψ, calculated as discussed

above. The slope of the curve Ψ vs. $\nu^{-1/2}$ plot was used for the calculation of k^0. The α value used in Eq. (2) was the same as that determined for the calculation of $K(\Lambda,\alpha)$.

$$\Psi = k^0 \bullet \left(\frac{D_O}{D_R}\right)^{\alpha/2} \bullet \left(\pi \bullet D_O \bullet \frac{n \bullet F}{R \bullet T} \bullet \nu\right)^{-1/2} \quad (2)$$

The potential window of the selected WEs in the negative potential region was determined based on a qualitative inspection of a series of CVs in HCF obtained by incrementally decreasing the lower vertex potential of the sweep range by 50 mV increments from −0.2 V to −1.5 V between subsequent scans. The limits of the potential range are identified as the onset potential of hydrogen evolution reaction (HER) at which the current was in the same range as the peak current of the HCF redox probe (i.e. approximately 1.0 mA).

The CVs of IMD and corresponding PBS measurements with selected WEs were recorded between −1.5 V and +0.6 V from the initial potential of 0.0 V in the positive direction with a step of 2.44 mV at scan rates of 5, 10, 20, 50, and 100 mV s^{-1}. Each fresh electrode was first conditioned by performing 5 cycles at 100 mV s^{-1} in PBS, followed by the recording of 3 cycles in PBS at all 5 given scan rates. Then 3 consecutive cycles were measured in 1000 μM IMD at 100 mV s^{-1}. Subsequently, one CV cycle was recorded in 1000 μM IMD at all 5 given scan rates. All measurements in IMD were performed after 1 min of accumulation at OCP under stirring conditions at 750 min^{-1}. To avoid memory effects, 3 CV cycles in PBS at 100 mV s^{-1} were performed after each measurement in IMD solution to remove any adsorbed species. The current peaks of the first cycle measured in IMD were characterised by evaluating i_p and E_p. The i_p values obtained at different scan rates were plotted against ν and $\nu^{1/2}$ to evaluate the reaction-limiting process, i.e., the adsorption- vs. diffusion-controlled mechanism.

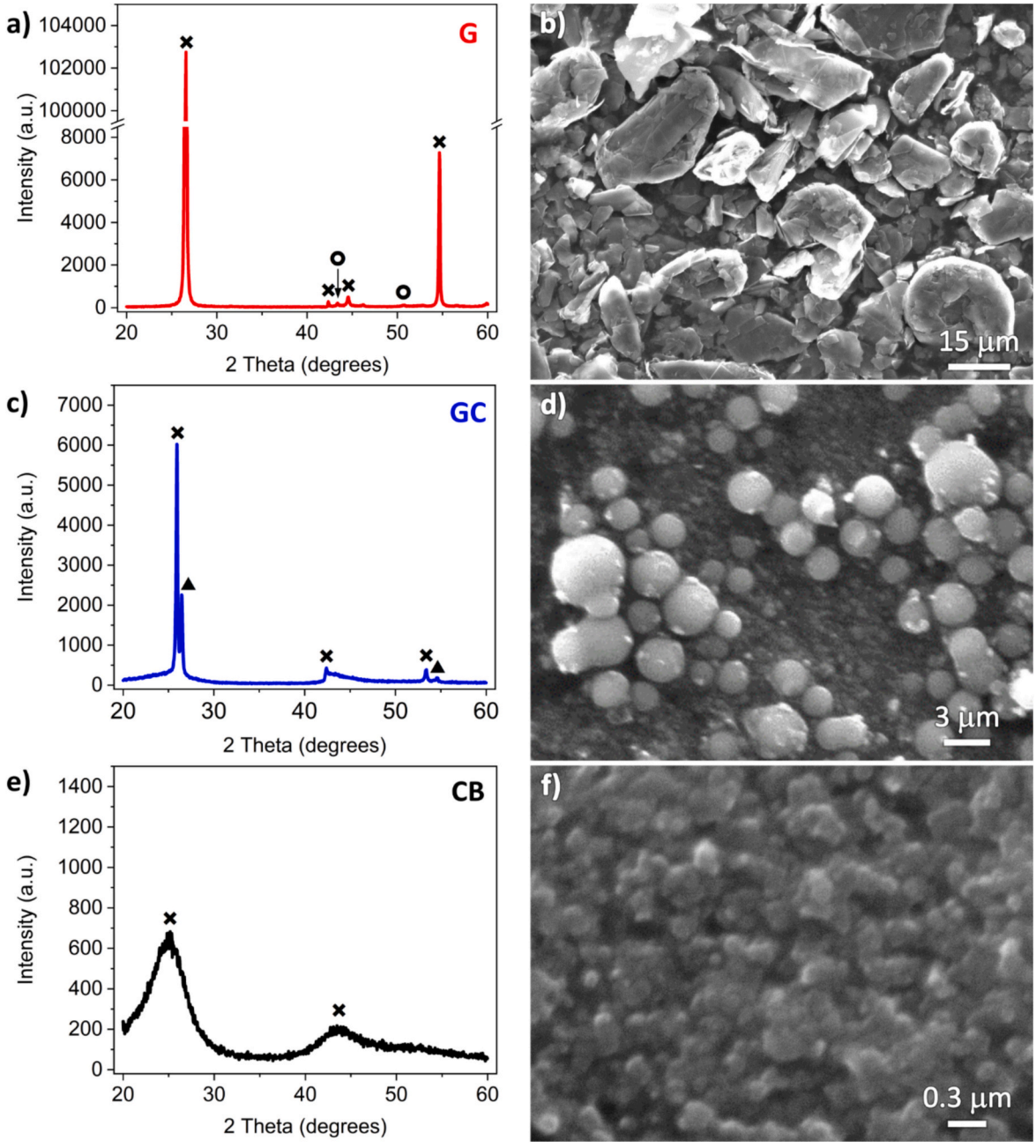

Fig. 3. XRD patterns and SEM images of the graphite (a, b), glassy carbon (c, d) and carbon black (e, f) powder. ✖: hexagonal graphite (PDF 00-56-0159), ○: cubic carbon (PDF 00–060-0053), ▲: hexagonal graphite (PDF 04–015-2407).

The CVs of selected WEs were recorded at 100 mV s^{-1} in IMD solution with concentrations of 1 μM, 10 μM, 100 μM and 1000 μM, starting with the lowest concentration to minimise possible memory effects. The i_p values at different IMD concentrations were used to obtain calibration curves and determine the limits of detection (LODs) as the IMD concentration at which the obtained i_{pc} exceeded the 3-fold value of the standard deviation of the blank (σ_{bl}).

3. Results and discussion

3.1. Properties of carbon powders

The XRD patterns of the G, GC, and CB powders are shown in Fig. 3a, c, e. The characteristic peaks of all carbon materials correspond to the hexagonal crystal structure of graphite (PDF 00-56-0159). The most pronounced peaks at 26.6° and 54.7° are the basal plane reflections, indexed as the reflexes (002) and (004), respectively, while 42.4° and 44.5° correspond to the two-dimensional (100) and (101) lattice reflections of crystalline graphite. In the XRD pattern of G (Fig. 3a), we additionally identified low-intensity peaks at ~43° and ~50°, attributed to a cubic structure of carbon (PDF 00-060-0053). In the XRD pattern of glassy carbon (Fig. 3c), we identified two strong diffraction peaks, well separated but close to each other, at ~26.5°, as well as two low-intensity peaks at ~54.5° and one peak at ~42°. They were indexed by hexagonal structures of graphite with slightly different unit cell size (PDF 00-56-0159, PDF 04-015-2407). The XRD diffraction pattern of the CB powder (Fig. 3e) is characterised by two broad, low-intensity peaks at ~25° and ~43°, and a relatively high background, which is characteristic of carbon black [37,38]. The broadening of the peaks could be correlated with the small particles, evident in the particle size distribution (Fig. S1c) and in the SEM image (Fig. 3f). On the other hand, the GC powder consists of a mixture of sub-micrometre-sized particles and a few micrometre-sized spherical particles (Fig. 3d), which is consistent with a bimodal particle size distribution with a fraction maximum at 0.7 μm and 3.3 μm (Fig. S1b). Particles of the G powder are platelet-shaped with a log-normal particle size distribution with a median of 15 μm (Fig. 3b, Fig. S1a).

3.2. Properties of carbon pastes

The pastes of G, GC, and CB were analysed by thermogravimetric analysis (TGA) to determine the post-deposition curing of the screen-printed layers. The TGA of the pastes conducted in an argon atmosphere (Fig. 4) shows that all 3 materials exhibit similar behaviour, as ~70 % of their initial mass is lost up to 1200 °C in two distinct steps. The first step takes place between room temperature and 200 °C, where ~60 % of the mass is lost. Upon further heating to 350 °C, additional ~11 % decrease in mass is observed. No mass change was recorded between 350 °C and 1200 °C. The mass loss up to 350 °C corresponds well to the amount of organic vehicle in the paste, namely 42 wt% of TPN, 17.5 wt % of BEEA and 10.5 wt% of EC. These results suggest that the entire amount of organic vehicle is eliminated from the pastes when they are heated to 350 °C in an argon atmosphere and that the ~30 wt% of G, GC, and CB remain thermally stable up to 1200 °C. Based on these results, the screen-printed layers were annealed at 450 °C to remove the organic vehicle and subsequently heated at 850 °C. This temperature was selected based on previous results showing that annealing graphite thick films at 850 °C leads to lower sheet resistances and an improved electrochemical response [19].

3.3. Thick film characterization

The G, GC, and CB thick films were black in colour, free of cracks and adhered well to the alumina substrate after annealing at 850 °C in argon. Furthermore, when these films were immersed and rinsed with water, they did not delaminate from the substrate, confirming their mechanical

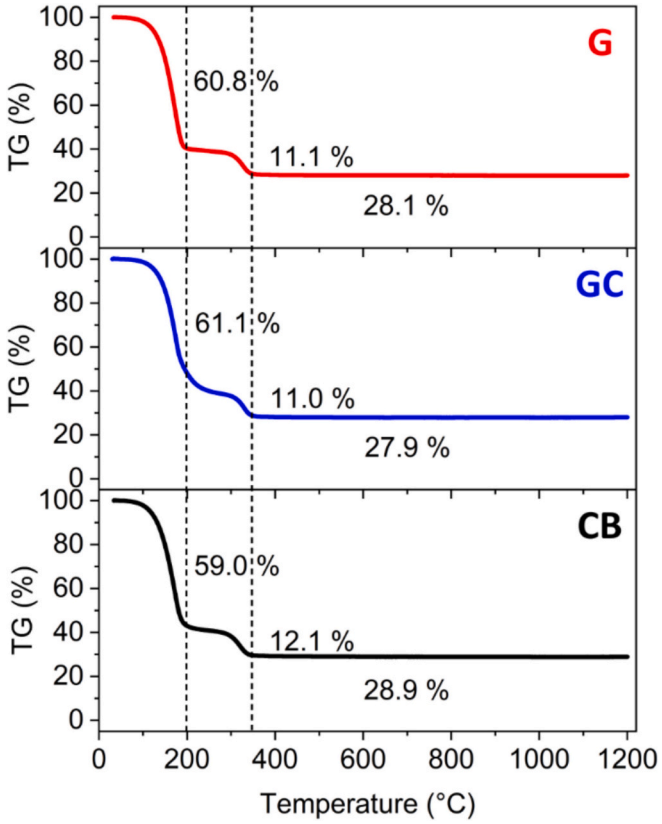

Fig. 4. TGA of graphite (G), glassy carbon (GC), and carbon black (CB) pastes between room temperature and 1200 °C in an argon atmosphere.

stability and suitability for electrochemical applications. From the thickness profiles (Fig. 5), it is evident that all films exhibited a uniform thickness over the entire length of the film. The thickness varied in the range of 25–40 μm for G, 18–22 μm for GC, and 19–22 μm for CB thick film and is in good agreement with the surface roughness R_q of the thick films (Table 1). The ability to integrate such high-quality films on alumina substrates, especially CB and GC, is indeed a remarkable novelty.

The SEM and AFM images of the surface of the G, GC, and CB thick films are shown in Fig. 6. The G thick film (Fig. 6a, b) exhibits a homogeneous surface with irregularly shaped, randomly orientated, a few tens of micrometre-sized flake-like particles, similar to the initial powder. This is reflected in the rough surface. The surface of GC consists of spherical particles up to ~5 μm in size, homogeneously distributed between particles less than one micrometre in size, which is reflected in a relatively smooth surface (Fig. 6c, d). The surface of CB is homogeneous with evenly distributed particles in the sub-micrometre range, which is reflected in the smoothest surface with the lowest R_q (Fig. 6e, f, Table 1).

Note that for all materials, the R_q determined from the thickness profiles are larger than the R_q^{AFM} determined from the AFM images (Fig. 6b, d, f). The differences in R_q could be related to the principles of measurement. The AFM measures the interaction forces between the tip and the surface to create a topographic map, while the profilometer records height deviations on the surface, providing information about the surface profile and roughness over larger areas than the AFM. In addition, a surface of 80 μm × 80 μm was examined with the AFM while a 6.5 mm long line was analysed with the profilometer. We hypothesise that examining a larger area would provide more representative values, especially for G with a rougher surface. In this case, the R_q^{AFM} was determined only for the dark area where the forces between the tip and the surface were measured (Fig. 6b). The light areas (LA) represent regions where the forces could not be measured due to higher roughness.

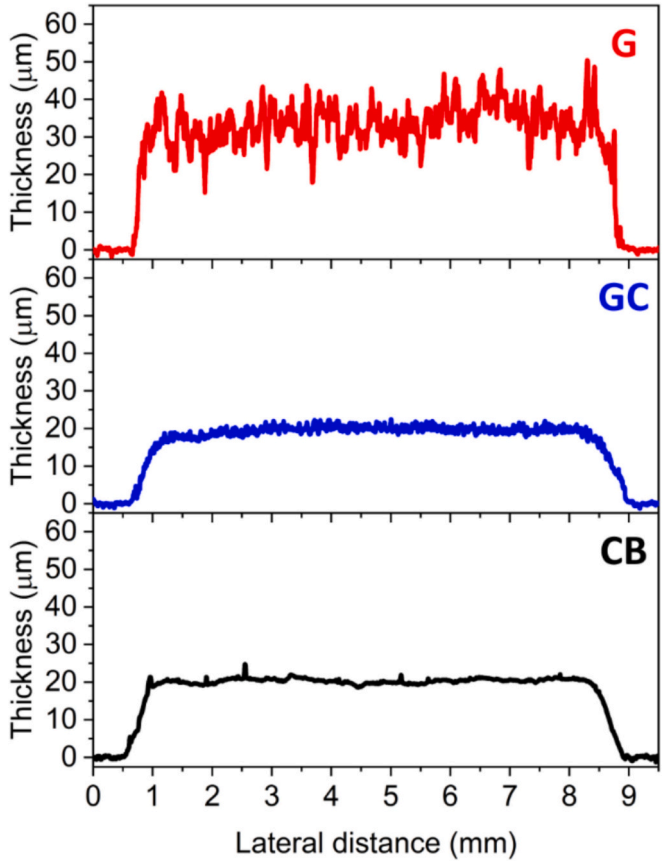

Fig. 5. Thickness profiles of graphite (G), glassy carbon (GC), and carbon black (CB) thick films on alumina fired at 850 °C in argon.

Table 1
Average thickness and roughness of G, GC, and CB thick films fired at 850 °C in argon.

	G	GC	CB
t [μm]	34.4 ± 0.9	18.7 ± 1.1	18.1 ± 1.1
R_q [μm]	3.7 ± 0.2	0.7 ± 0.1	0.4 ± 0.1
R_q^{AFM} [μm]	2.1*	0.56	0.07

* Determined from the smooth region.

Consequently, the R_q^{AFM} was lower and could even be considered incorrect, than the results obtained with the profilometer.

The sheet resistance of the G, GC, and CB thick films measured at room temperature was the lowest for the G thick films, 6.9 ± 0.4 Ω/sq. Higher and comparable sheet resistances were determined for GC and CB thick films with 27 ± 1 Ω/sq and 21 ± 1 Ω/sq, respectively. The lower sheet resistance of G thick films can be attributed to the graphite structure, as it crystallises in a hexagonal structure with layers of carbon atoms (Fig. 3a). The delocalised electrons can therefore move in these layers and contribute to higher electrical conductivity. On the other hand, CB consists of nano-sized grains with low-intensity, broad diffraction peaks of the hexagonal structure (Fig. 3e). Its layered structure has lower level of order and consequently the mobility of electrons is slower than in G. The GC thick films had the highest resistivity, although they are crystalline (Fig. 3c) and contain micrometre-sized particles.

We demonstrated that by managing each processing step, we can produce G, GC, and CB films on alumina substrates with high performances. The different particle size distributions of the starting powders used in the fabrication of the self-developed screen-printing paste led to different surface morphologies in the resulting films, as shown by SEM and AFM images. Annealing at 850 °C in an argon atmosphere resulted in homogeneous films with high conductivity and a sheet resistance of less than 27 Ω/sq. Notably, the conductivity appears to be largely unaffected by variations in the crystal structure of the starting powders.

3.4. Functional properties

3.4.1. Electrochemical response to redox probe

The CVs measured for the HCF redox probe using WE made from G, GC, and CB thick film are shown in Fig. 7 and the evaluation of their properties is summarised in Table 2. It can be seen that all electrodes exhibit similar behaviour, with good reversibility of the redox process with i_{pc}/i_{pa} close to unity and a similar $E_{1/2}$ of ~0.22 V. G and GC exhibit comparable i_{cap} and ΔE_p. However, G shows a higher P/B current ratio than GC. CB has significantly larger i_{cap}, the smallest P/B current ratio and the largest ΔE_p. The CVs recorded at different scan rates with G, GC, and CB used as WEs, with the plots of i_p vs. $\nu^{1/2}$ as insets, are shown in Fig. S2, and the E_p, $E_{p/2}$ and ΔE_p at various scan rates are listed in Table S1, both in Supporting information. The linear relationship between i_p and $\nu^{1/2}$ indicates that the redox process is controlled by the diffusion of the electroactive species in all cases. A common method to determine whether the redox system is adsorption- or diffusion-controlled is also to analyse the dependence of the peak current on the scan rate. The relationship between the logarithm of the peak current ($\log i_p$) and the logarithm of ν ($\log \nu$) gives a linear dependence with the gradient of 0.5 for a purely diffusion-controlled and of 1 for a purely adsorption-controlled system [39,40]. The slopes of the plot of $\log |i_p|$ vs. $\log |\nu|$ (not shown), where i_p represents the average value of absolute i_{pa} and i_{pc}, were 0.61 ($R^2 = 0.9989$), 0.51 ($R^2 = 0.9992$), and 0.48 ($R^2 = 0.9905$) for G, GC, and CB, respectively. For CB and GC, the slope is around 0.5, indicating that the process is mainly controlled by the diffusion of the electroactive species, while the slope of G indicates a mixed system with non-negligible adsorption in addition to a diffusion-controlled system. The CVs measured at different scan rates (Fig. S2) were also used for the determination of A_{ecsa}. Since the peak potentials depend on the scan rate, and $n\Delta E_p$ ranged between 63 mV and 212 mV for majority of the measurements (Table S1), we assume electrochemically quasi-reversible reaction. The A_{esca} was thus calculated based on the modified Randles-Ševčík equation (Eq. (1)) [32]. The largest value of A_{ecsa} was found for G with the platelet-shaped particles and the highest surface roughness, while GC and CB, which have a smoother surface and similar R_q, exhibited similar A_{ecsa} values, as expected. However, when comparing the current densities of the cathodic and anodic processes (j_{pc} and j_{pa}, respectively), the highest value is obtained for CB. The CB thick film consists of sub-micrometre-sized particles, which have a higher surface-to-volume ratio and provide more active sites for the reactants to interact with the electrode compared to other two materials. A mean value is observed for GC with a few micrometre-sized spherical particles, while the lowest value was found for G. The plot of Ψ vs. $\nu^{-1/2}$ for the determination of k^0 is shown in Fig. S2d. The highest k^0 value was obtained for G with the highest electrical conductivity. Although the GC layers have a higher resistance than the CB layers, a higher k^0 value was determined for GC, possibly due to a more crystalline structure, that could be favourable for faster charge transfer. Considering the electrochemical properties of integrated G, GC, and CB, all these materials have been promising candidates for the detection of IMD.

Table 3 summarises the A_{real} and k^0 values for different electrodes: G, GC, and CB. We collected A_{esca} and k^0 values from the literature, which were obtained through cyclic voltammetry at various scan rates using the $[Fe(CN)_6]^{3-/4-}$ redox probe, similar to our measurement approach. Additionally, A_{esca} was normalised with the geometric surface area to calculate the actual surface area, A_{real} expressed in cm^2/cm^2_{geo}. It is evident that the A_{real} of commercially available graphitic electrodes is much smaller than that of our samples, even though their roughness levels are similar. The surface roughness of commercial electrodes varies between 0.65 and 2.52 μm. The electrodes discussed in this study exhibit

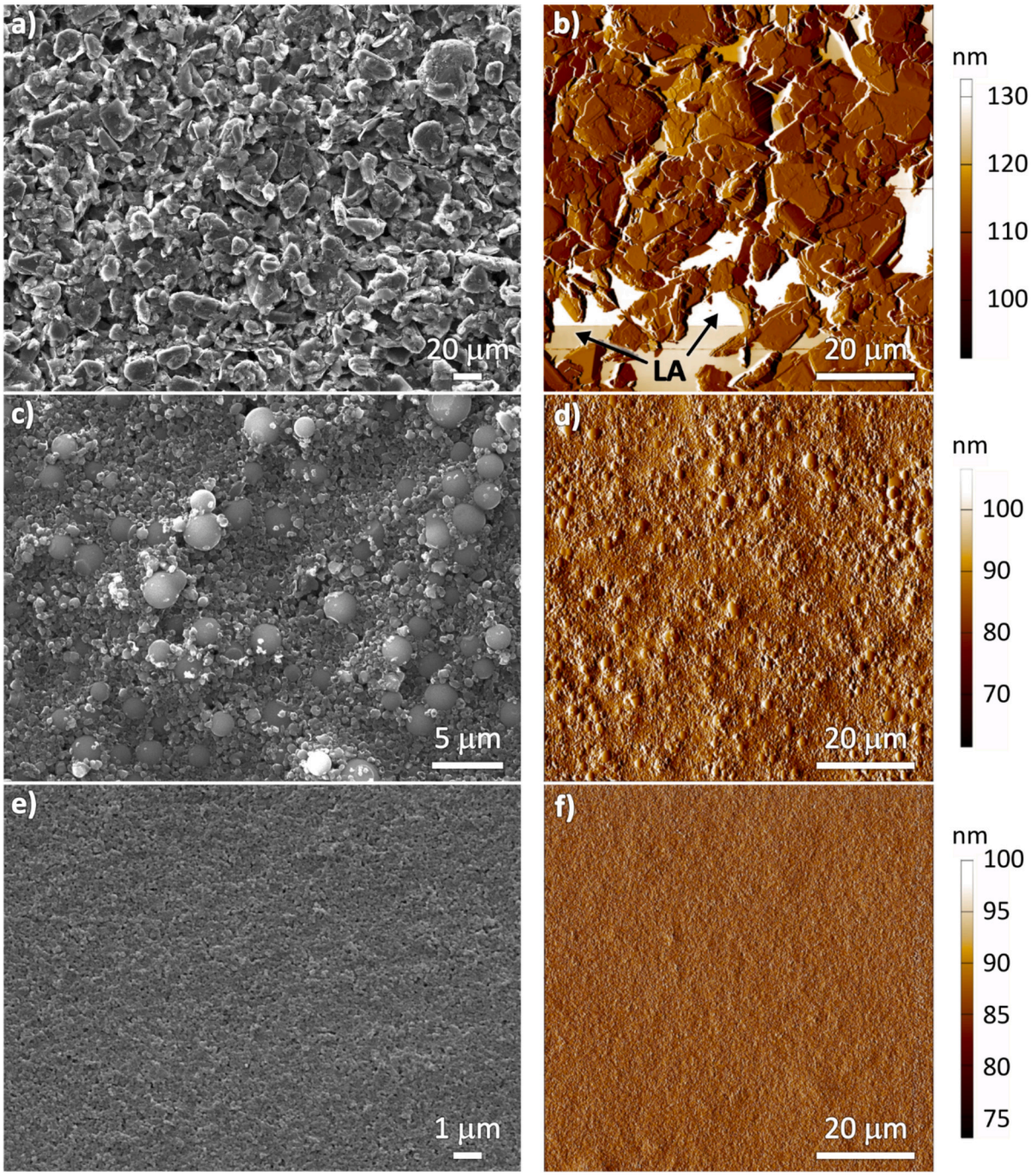

Fig. 6. SEM and AFM images of graphite (a, b), glassy carbon (c, d), and carbon black (e, f) thick films. LA: light area, where the forces between the tip and the surface could not be measured.

k^0 values within the same range as commercial electrodes [36]. It was shown that electrochemical pretreatment of the WE can enhance its electroanalytical properties, resulting in an increased k^0 value [12,41,42]. However, the graphite electrodes reported in this work, which were assessed in their as-prepared state without any further electrochemical pretreatment, exhibited the highest A_{real} and k^0 values compared to other screen-printed [31,43,44] and aerosol-deposited [45] graphite electrodes.

Reports of integrated GC or CB materials are rare in the literature. Most GC reported are glassy carbon disc electrodes (GCE) [43,46,47]. In these articles A_{esca} was not reported, while the k^0 ranged from 0.3 to 12 $\times$ 10^{-3} cm s^{-}1. The screen-printed GC-based electrodes were prepared from a mixture of GC powder and polyvinyl chloride solution in cyclohexanone and paraffin oil [48], and from a composite mixture of GC powder and commercially available carbon ink (GC-carbon ink) [24,25]. In addition, the GC films were prepared by chemical vapour deposition [49]. However, the electrochemical properties were not specified for any of them.

On the contrary, carbon black is primarily utilised as a modifier applied through drop-casting onto integrated graphite WEs [27,50–53]. The modification of graphite electrodes with CB enhance their response, as evident by an increased k^0 value and a reduced charge transfer resistance (R_{ct}) determined by electrochemical impedance spectroscopy [50,51,53]. However, the current response strongly depends on the particle size and morphology of the CB powder used for the modification, as well as the base electrode itself, as shown in reviews [26,27].

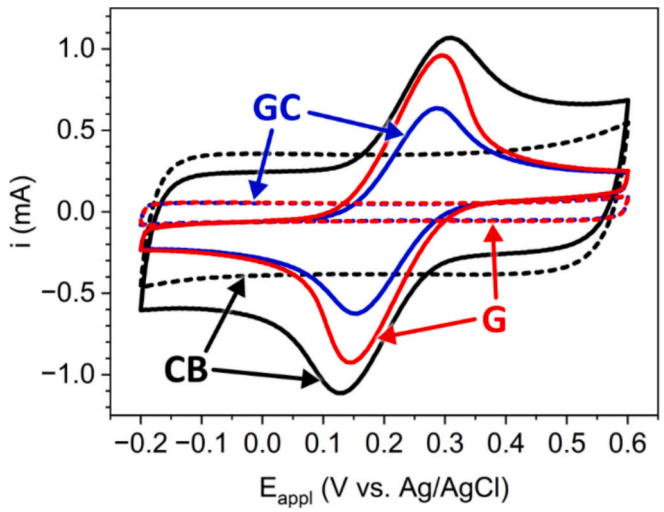

Fig. 7. Cyclic voltammograms using G, GC, and CB as WE, recorded in 0.1 M PBS (blank, dashed lines) and 5 mM HCF in 0.1 M PBS supporting electrolyte (solid lines) at 100 mV s^{-1} between −0.2 V and +0.6 V from initial potential 0.0 V in the positive direction.

Table 2
Summary of the electrochemical properties of the G, GC, and CB thick film as WE obtained from the CVs recorded in 5 mM HCF in 0.1 M PBS.

	G	GC	CB
i_{cap} [mA]	113 ± 2	107 ± 6	755 ± 21
P/B current ratio	16 ± 1	11 ± 1	1.9 ± 0.1
i_{pc}/i_{pa}	0.958 ± 0.001	0.958 ± 0.014	1.023 ± 0.004
$E_{1/2}$ [mV]	218 ± 1	221 ± 1	220 ± 1
ΔE_p [mV]	143 ± 8	138 ± 7	177 ± 3
A_{ecsa} [cm^2]	2.51 ± 0.15	1.30 ± 0.01	1.26 ± 0.01
$-j_{pc}$ [mA/cm^2]	0.352 ± 0.019	0.440 ± 0.002	0.562 ± 0.007
j_{pa} [mA/cm^2]	0.368 ± 0.020	0.459 ± 0.009	0.549 ± 0.005
k^0 [10^{-3} cm/s]	4.3 ± 0.5	3.5 ± 0.4	2.5 ± 0.2

Table 3
A_{real} and k^0 for different graphite (G), glassy carbon (GC) and carbon back (CB) electrodes.

WE material	A_{real} [cm^2/cm^2_{geo}]	k^0 [10^{-3} cm/s]	[reference]
SP G, C110 (Drop Sens)	0.79	6.2	[36]
SP G, KS 530 (Kanichi)	0.69	1.2	[36]
SP G, TE100 (Zensor)	0.49	0.25	[36]
SP G	3.92 ± 0.23	4.3 ± 0.5	This work
SP G	0.3	0.401 ± 0.022	[31]
SP G	/	2.2	[43]
SP G	/	3.2 ± 0.2	[44]
AD G	1.44 ± 0.06	1.9	[45]
SP GC	2.03 ± 0.01	3.5 ± 0.4	This work
GCE	/	12	[43]
GCE	/	0.279	[46]
GCE	/	0.369	[47]
SP CB	1.97 ± 0.01	2.5 ± 0.2	This work
CB – SP G	/	4.52	[52]
CB – SP G	/	15.9	[50]
CB – SP G	/	20 ± 2	[51]

SP – screen-printed, AD – aerosol-deposited, GCE – glassy carbon disc electrode.

Although the k^0 value reported for CB in this study is lower than that for graphite WEs modified with CB, it reflects the response characteristics of a pristine, unmodified CB electrode. CB has also been used for the preparation of carbon black paste electrodes [54–56], composite CB-carbon ink, CB-G ink and CB-cellulose acetate inks for the fabrication of integrated electrodes [51,57], but their A_{ecsa} and k^0 values have not been evaluated.

Since the stability of the electrode at high negative potentials is crucial for the detection of IMD and other NNIs, special attention was paid to the investigation of the potential window at negative potentials on the investigated films in PBS by gradually decreasing the lower vertex potential. It was confirmed that all three electrodes, namely G, GC and CB, could withstand potential cycles down to −1.5 V, with the onset potential for HER at around −1.2 V for all three electrode materials, allowing detection of the IMD reduction peak at around −1.1 V.

3.4.2. *Electrochemical detection of imidacloprid*

The CVs measured in 1000 μM IMD solution after 1 min of accumulation at OCP under stirring conditions with the corresponding measurements in PBS (without accumulation) are shown in Fig. 8. When G and GC were used as WE, a single and relatively broad cathodic peak was observed at about −1.1 V (C1), which corresponds to the reduction of the nitro functional group of IMD to hydroxylamine [11]. The peak observed using G is more pronounced and has a higher i_{pc1} compared to GC, where the peak also appears to be lower and broader. On the other hand, two overlapping cathodic peaks (marked as C1 and C2) can be observed when CB was used as WE. The first reaction (C1) leads to the formation of a shoulder superimposed with a response of the second reduction peak (C2). Since the shoulder occurs at the same peak potential as the C1 observed at the other two electrodes, it could be attributed to the same reduction process, i.e., the reduction of the nitro group. The second cathodic peak (C2) appears at a more negative potential of about −1.4 V and is significantly higher than C1. Since such high currents were not observed for HER in blank PBS (Fig. 8), C2 can be attributed to a different faradaic process, which is additionally

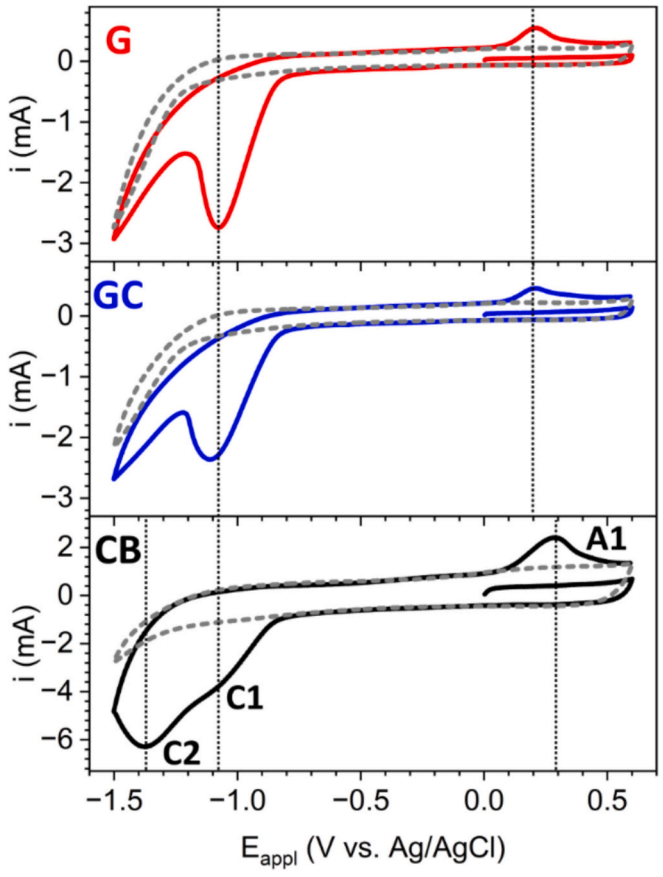

Fig. 8. Cyclic voltammograms using G, GC, and CB as WE, recorded in 0.1 M PBS (dashed lines) and in 1000 μM IMD in 0.1 M PBS supporting electrolyte (solid lines) at 100 mV s^{-1} between −1.5 V and +0.6 V from initial potential 0.0 V in positive direction.

supported by a significantly different signal shape (onset of a current peak). Since the measurements were recorded after 1 min of accumulation, it is possible to assume that C2 corresponds to the reduction of adsorbed IMD, which requires higher reduction overpotentials compared to dissolved species. This was additionally confirmed by recording CV immediately after immersing the electrodes in the solution, i.e., without a 1-min accumulation process (Fig. S4). In this case, only one cathodic peak, namely C1, was observed, confirming that there was not enough time for IMD adsorption. The 30 %, 19 %, and 28 % increase in i_{pc1} observed after 1-min accumulation compared to the measurement without accumulation on G, GC, and CB, respectively, demonstrates a potential benefit of accumulation for improved sensitivity and thus lower LODs, particularly in the case of significantly lower environmentally relevant concentrations. However, the optimization of accumulation time was not the main objective of this work, but served to gain a deeper understanding of the mechanism of the reaction process and to improve the reproducibility of the results. Since peak C2 was the most pronounced signal obtained with CB, these results suggest that CB has the highest adsorption affinity for IMD among the investigated electrode materials. However, due to the relatively broad peaks C1 recorded on GC and G, it is possible that adsorption also occurred on these materials, but the overpotential for the reduction of adsorbed IMD overlapped with the reduction of dissolved IMD species. During the positive potential scan, an anodic peak (A1) was also observed on all three WEs at approximately +0.2 V for G and GC, and at +0.3 V for CB. Since the peak was not detected during the first forward scan, i.e., before the reduction of IMD, it can be explained by the re-oxidation of the product(s) formed during the C1 and C2 processes. This was verified by stirring the solution during the second positive potential sweep (after recording C1) below 0.0 V, resulting in the absence of peaks A1 on G and GC, which reappeared in the next positive scan (recorded without stirring), as shown in Fig. S4. Since the peak was not recorded on G and GC in the case of stirring the solution in the second semi-cycle, this indicates that the species reduced during the C1 process are not adsorbed on the surface of G and GC. On the other hand, stirring the solution did not entirely remove the adsorbed species from CB, as the current A1 was still observed (Fig. S4c, solid line), indicating a much stronger adsorption interaction of the reduced IMD product on the surface of CB, as predicted above. To the best of our knowledge, this is the first report of an anodic re-oxidation peak for NNIs utilising a carbon-based WE. This result emphasises the novel potential of carbon materials to improve our understanding of sensing NNIs.

In order to compare the observed peak currents in the IMD solution using electrode materials with different A_{ecsa}, the peak current densities were calculated and are summarised in Table 4. When comparing the peak current densities of C1 (j_{pc1}), the highest values were found for CB, followed by GC and G, similar to what was observed for the HCF redox probe. The peak current density of the C2 process (j_{pc2}) observed on CB is even higher than j_{pc1}. It is noteworthy that when 3 consecutive CV scans are performed in 1000 μM IMD solution after 1 min of accumulation (without stirring the solution between cycles), as shown in Fig. S5, a broader C1 current peak and the appearance of the peak C2 on CB are observed only in the first scan. This further confirms that the processes causing this phenomenon could be related to the reduction of adsorbed IMD, as the IMD did not have enough time to adsorb on the electrode surface between scans, since the 1-min preconcentration step was only applied before the first cycle. There is also a considerable decrease of both C1 and A1 peak currents in the second CV cycle compared to the first scan. The cathodic and anodic peak currents in the second cycle were only 49 %, 59 %, and 55 % of the initial i_{pc1} and 58 %, 63 % and 50 % of the initial i_{pa1} for G, GC and CB, respectively. Subsequent scans exhibited a much smaller decrease, indicating a stabilization of the current signals after the second cycle. Similar behaviour was also observed for the CVs recorded without accumulation (not shown). Therefore, the significantly lower currents in the second and later scans are most likely related to a diffusion gradient due to the decreased concentration of analyte in the vicinity of the electrode, which is in accordance with the irreversible reaction mechanism of IMD. However, there are also reports of such behaviour being attributed to the occupation of the active sites on the WE surface by the adsorbed oxidised products [58]. The re-oxidation peak A1 confirms that some oxidised species are formed during the A1 process.

Table 4
Summary of the peak current densities of CVs recorded in 1000 μM IMD solution in 0.1 M PBS supporting electrolyte at 100 mV s^{-1} on G, GC and CB thick-film WEs.

	G	GC	CB
j_{pa1} [mA/cm^2]	0.22	0.35	1.78
j_{pc1} [mA/cm^2]	−1.09	−1.81	−2.94
j_{pc2} [mA/cm^2]			−5.01

Further information on the reaction mechanism was obtained from the CVs recorded with G, GC, and CB at different scan rates, including the dependence of i_{pc} on $\nu^{1/2}$ and i_{pa} on ν, as shown in Fig. S6. Since two cathodic peaks were observed on CB, both i_{pc1} and i_{pc2} were determined by subtracting the capacitive current without deconvolution and plotted against $\nu^{1/2}$. The ratio between i_{pc1} and i_{pc2} changed with scan rates, with C1 being predominant at slower ν, while C2 became increasingly dominant at faster ν. Both peaks show linear behaviour with $\nu^{1/2}$, with C2 having a slope approximately 2 times larger. All cathodic peak currents increase linearly with $\nu^{1/2}$ for all electrode materials, suggesting that the redox processes C1 and C2 are diffusion-controlled. This was further confirmed by the slopes of log $|i_{pc}|$ vs. log $|\nu|$ (not shown), which were 0.48 ($R^2 = 0.9964$), 0.43 ($R^2 = 0.9950$) and 0.32 ($R^2 = 0.9931$) for i_{pc1} on G, GC, and CB, respectively, indicating a purely diffusion-controlled process C1, while the slope for i_{pc2} on CB was 0.60 ($R^2 = 0.9833$), which indicates a mixed system with both adsorption- and diffusion-controlled redox process. On the other hand, the anodic peak currents increase linearly with ν for all materials, suggesting that the redox process A1 is adsorption-controlled for all carbon electrodes. Again, the slopes of log $|i_{pa1}|$ vs. log $|\nu|$ (not shown) of 1.03 ($R^2 = 0.9979$), 1.03 ($R^2 = 0.9971$) and 0.84 ($R^2 = 0.9957$) for G, GC and CB, respectively, confirm that this process is purely controlled by adsorption for G and GC, while a mixed system with adsorption predominance is obtained for CB. Since cathodic peaks (C1 and C2) are higher and more pronounced than A1, they are generally more suitable for the detection of IMD. However, the use of the re-oxidation peak A1 could be of importance in case of interreferences due to complex matrix and/or sensor systems without purging, e.g., on-field detection with flow-through systems. Its diffusion-dependent mechanism further emphasises the importance of the accumulation process for improved sensitivity.

Fig. 9 shows CVs recorded using G, GC, and CB as WE in IMD solution at different concentrations from 1 μM to 1000 μM. At concentrations lower than 1000 μM, only one cathodic peak was obtained at all three electrodes. The indistinct C2 peak on CB at lower concentrations could be explained by the lower adsorption efficiency at lower concentrations of IMD, which requires a longer accumulation time to further increase the C2 current and thus improve the detection. However, compared to the other two electrode materials, the peak C1 on CB is significantly broader at all studied concentration levels, which could be a further indication of an accompanying adsorption process. As demonstrated in the insets in Fig. 9, it was possible to obtain a measurable signal for IMD even at a concentration of only 1 μM on all three electrodes. The intensities of i_{pc1} are higher than the 3-fold value of the standard deviation of the blank value (σ_{bl}). Fig. 9d shows the dependence of the absolute value of i_{pc} on the concentration of IMD for the G, GC, and CB WE. G and GC show a similar behaviour with a linear dependence of log i_{pc} on the log c plot between 1 and 100 μM, while at 1000 μM IMD the recorded currents deviate from the linear dependence. In contrast, i_{pc} obtained on CB exhibits a linear relationship with concentration over the entire

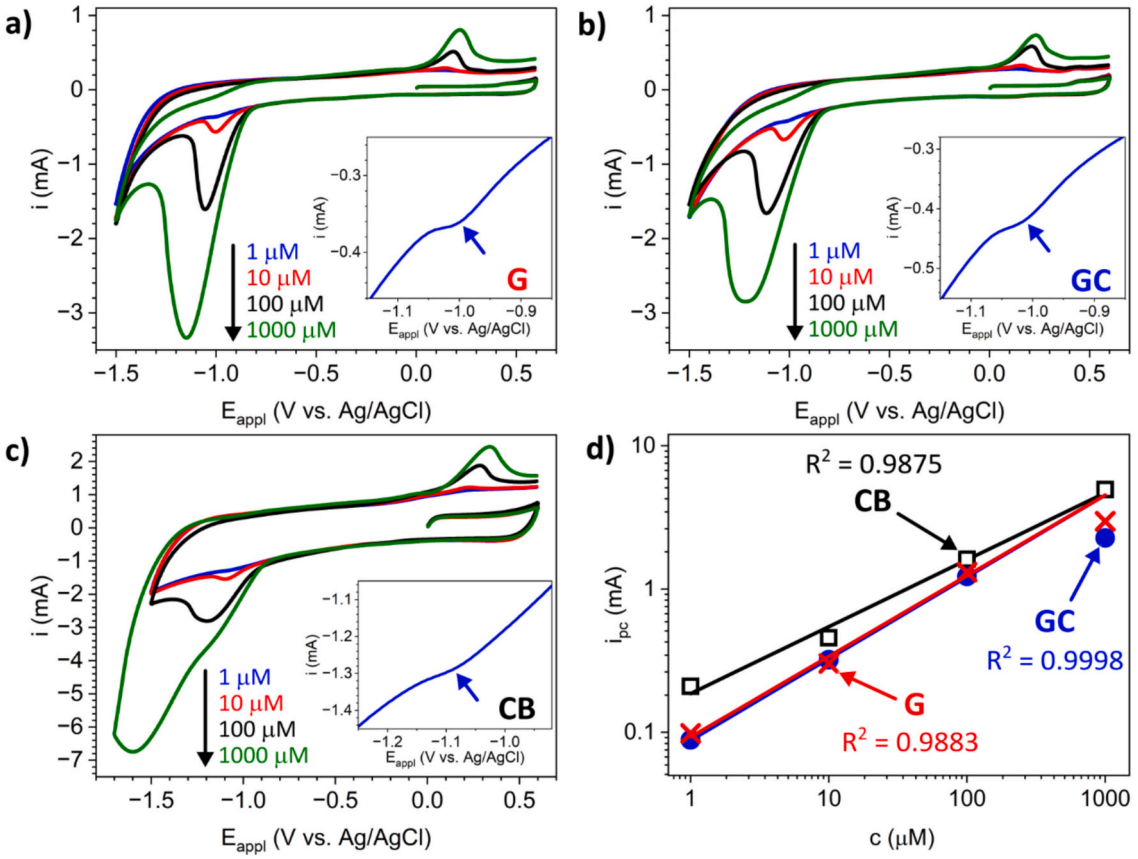

Fig. 9. Cyclic voltammograms recorded in 1 µM, 10 µM, 100 µM, and 1000 µM IMD solution in 0.1 M PBS supporting electrolyte at 100 mV s^{-1} between −1.5 V and +0.6 V from initial potential 0.0 V in positive direction after 1 min accumulation (under stirring conditions) using different WE materials: a) G, b) GC and c) CB. The insets (blue curves) show the measurement in 1 µM IMD solution. d) Plot of log i_{pc} vs. log c for G (red cross), GC (blue circle), and CB (black square) thick-film WE. For GC and G, the R^2 values were determined for the linear range, i.e., for concentrations below 100 µM. (For interpretation of the references to colour in this figure legend, the reader is referred to the web version of this article.)

concentration range investigated, i.e., 1–1000 µM, indicating a broader linear range for IMD detection using CB electrode material. In addition, the i_{pc} values obtained on CB are slightly higher compared to those obtained on the other two electrodes, with significant difference at the lowest concentration (1 µM). There are only a few papers that report on the limit of detection (LOD) values determined using the linear scan technique. For pristine bulk glassy carbon electrodes (GCEs), the LOD value for IMD is around 30 µM, while for more sensitive techniques, namely square wave voltammetry, a lower LOD value of 11 µM is reported [59,60]. The LOD values reported in this paper for G, GC and CB are about 10-times lower, i.e., in the range of 1 µM. The LODs reported for modified GCE are even lower, down to 0.02 µM [61–66] and similar concentration range is reported for electrochemically pretreated GCE using pulsed techniques [12]. From these results, we conclude that the integrated G, GC, and CB are effective for detecting IMD at concentrations as low as 1 µM using CV and, moreover, offer a great potential for further sensors development based on pulsed methods for obtaining lower LODs. Among investigated materials, CB showed the highest sensitivity which is mainly related to the concomitant adsorption process, based on the high adsorption affinity of IMD towards the CB surface. Accumulation and thus preconcentration of the analyte can be further utilised to achieve even lower LODs, particularly in combination with more sensitive pulsed techniques.

In this study, we demonstrate the successful processing of homogeneous, crack-free thick films of G, GC and CB on alumina from our self-developed pastes under optimised screen printing and annealing conditions. The produced thick films, including materials GC and CB that are rarely used for screen-printed electrodes, enable the detection of IMD. In addition, they achieve a sensitivity for IMD of 1 µM determined by cyclic voltammetry (CV), in their pristine and unmodified state. This opens up possibilities for their application in the development of miniature integrated electrochemical sensors.

4. Conclusions

This work has shown that well-adhered and conductive graphite (G), glassy carbon (GC), and carbon black (CB) thick films can be prepared by screen printing and subsequent annealing at 850 °C in argon. Sheet resistances below 27 Ω/sq were achieved for all carbon materials. The morphology of the films is greatly dependent on the particle size of the starting powder material. Larger G particles resulted in a higher surface roughness and consequently a higher electrochemically active surface area, while similarly lower values were obtained for GC and CB. The higher conductivity of G resulted in a higher heterogeneous electron transfer rate, although the values for all electrodes were in a similar range to those reported in the literature for integrated electrodes. CB stands out by having a relatively high capacitive current, resulting in less pronounced current peaks, however the peak current density at this electrode is the highest. This can be attributed to the sub-micrometre-sized particles exhibiting a higher surface-to-volume ratio. All three electrodes display the required stability between −1.5 V and +0.6 V, allowing both the cathodic and anodic detection of imidacloprid (IMD). A characteristic peak of reduction of the amino functional group at −1.1 V and a re-oxidation peak at +0.2 V were obtained at all three electrodes, while CB also exhibited an additional cathodic peak at −1.4 V. It has been demonstrated that the latter is due to the reduction of adsorbed

IMD, which is due to significantly higher affinity of CB for IMD adsorption compared to G and GC. Our results show that with a 1-min accumulation-based preconcentration step under stirring conditions all investigated carbon-based electrodes enable the detection of IMD at concentrations as low as 1 μM. Further optimization of the accumulation parameters and the application of other (pulsed) techniques could additionally enhance the sensitivity and significantly improve the detection limits for IMD utilising the investigated carbon-based thick-film electrodes for sensor applications.

CRediT authorship contribution statement

Barbara Repič: Writing – original draft, Visualization, Validation, Investigation, Formal analysis. **Gregor Marolt:** Writing – review & editing, Validation, Supervision, Methodology. **Danjela Kuscer:** Writing – review & editing, Writing – original draft, Visualization, Supervision, Resources, Project administration, Methodology, Investigation, Funding acquisition, Conceptualization.

Declaration of competing interest

The authors declare the following financial interests/personal relationships which may be considered as potential competing interests: Danjela Kuscer reports financial support was provided by Slovenian Research and Innovation Agency. Gregor Marolt reports financial support was provided by Slovenian Research and Innovation Agency. Barbara Repic reports financial support was provided by Slovenian Research and Innovation Agency. Danjela Kuscer reports financial support was provided by Ministry of Higher Education, Science and Innovation of Republic Slovenia. If there are other authors, they declare that they have no known competing financial interests or personal relationships that could have appeared to influence the work reported in this paper.

Acknowledgments

This work was funded by the Slovenian Research and Innovation Agency through the research projects P2 − 0105, J2 − 3049, P1 − 0153, and the Ministry of Higher Education, Science and Innovation of Republic Slovenia (C3360 − 23 − 252004, M − ERA.NET).

The authors thank Miha Nosan for performing the TG analysis and Hana Uršič for performing the AFM analysis.

Appendix A. Supplementary data

Supplementary data to this article can be found online at https://doi.org/10.1016/j.jelechem.2025.119054.

References

[1] N. Simon-Delso, V. Amaral-Rogers, L.P. Belzunces, J.M. Bonmatin, M. Chagnon, C. Downs, L. Furlan, D.W. Gibbons, C. Giorio, V. Girolami, et al., Systemic insecticides (neonicotinoids and Fipronil): trends, uses, mode of action and metabolites, Environ. Sci. Pollut. Res. 22 (2015) 5–34, https://doi.org/10.1007/s11356-014-3470-y.

[2] D.A. Thompson, H.-J. Lehmler, D.W. Kolpin, M.L. Hladik, J.D. Vargo, K. E. Schilling, G.H. LeFevre, T.L. Peeples, M.C. Poch, L.E. LaDuca, et al., A critical review on the potential impacts of neonicotinoid insecticide use: current knowledge of environmental fate, toxicity, and implications for human health, Environ Sci Process Impacts 22 (2020) 1315–1346, https://doi.org/10.1039/C9EM00586B.

[3] K. Kaewket, K. Ngamchuea, Microporous carbon for fast and simple electrochemical detection of Imidacloprid insecticide in fruit and water samples, RSC Adv. 13 (2023) 4532–4541, https://doi.org/10.1039/D3RA00192J.

[4] A. Navalón, R. El-Khattabi, A. González-Casado, J.L. Vilchez, Differential-pulse Polarographic determination of the insecticide Imidacloprid in commercial formulations, Mikrochim. Acta 130 (1999) 261–265, https://doi.org/10.1007/BF01242914.

[5] A. Guiberteau, T. Galeano, N. Mora, P. Parrilla, F. Salinas, Study and determination of the pesticide Imidacloprid by square wave adsorptive stripping voltammetry, Talanta 53 (2001) 943–949, https://doi.org/10.1016/s0039-9140(00)00576-2.

[6] V. Guzsvány, M. Kádár, F. Gaál, K. Tóth, L. Bjelica, Rapid differential pulse Polarographic determination of Thiamethoxam in commercial formulations and some real samples, Microchim. Acta 154 (2006) 321–328, https://doi.org/10.1007/s00604-006-0487-z.

[7] B. Barton, N. Ullah, K. Koszelska, S. Smarzewska, W. Ciesielski, D. Guziejewski, Reviewing neonicotinoid detection with electroanalytical methods, Environ. Sci. Pollut. Res. 31 (2024) 37923–37942, https://doi.org/10.1007/s11356-024-33676-1.

[8] D. Gonçalves-Filho, C.C.G. Silva, D. De Souza, Pesticides determination in foods and natural waters using solid amalgam-based electrodes: challenges and trends, Talanta 212 (2020) 120756, https://doi.org/10.1016/j.talanta.2020.120756.

[9] L. Ding, J. Guo, S. Chen, Y. Wang, Electrochemical sensing mechanisms of neonicotinoid pesticides and recent Progress in utilizing functional materials for electrochemical detection platforms, Talanta 273 (2024) 125937, https://doi.org/10.1016/j.talanta.2024.125937.

[10] V. Hegde, M.P. Bhat, J.-H. Lee, M.D. Kurkuri, C.S. Kim, K.-H. Lee, Carbon-based nanomaterials: multifaceted role in agrochemical recognition, remediation, and release, Nano Today 57 (2024) 102388, https://doi.org/10.1016/j.nantod.2024.102388.

[11] M.R. Smyth, J.G. Osteryoung, A pulse Polarographic investigation of parathion and some other nitro-containing pesticides, Anal. Chim. Acta 96 (1978) 335–344, https://doi.org/10.1016/S0003-2670(01)83670-9.

[12] Y. Lv, J. Sun, S. Qiao, M. Zhang, J. Li, A facile, inexpensive and green electrochemical sensor for sensitive detection of Imidacloprid residue in Rice using activated electrodes, Anal. Methods 13 (2021) 3649–3658, https://doi.org/10.1039/D1AY00984B.

[13] C. Zhang, Y. Li, N. Yang, M. You, J. Hao, J. Wang, J. Li, M. Zhang, Electrochemical sensors of neonicotinoid insecticides residues in food samples: from structure to analysis, Talanta 267 (2024) 125254, https://doi.org/10.1016/j.talanta.2023.125254.

[14] E. Cevik, A. Cerit, H. Tombuloglu, H. Sabit, H.B. Yildiz, Electrochemical glucose biosensors: whole cell microbial and enzymatic determination based on 10-(4H-Dithieno[3,2-b,2′,3′-d]Pyrrol-4-Yl)Decan-1-Amine interfaced glassy carbon electrodes, Anal. Lett. 52 (2019) 1138–1152, https://doi.org/10.1080/00032719.2018.1521828.

[15] D. Kuscer, in: M. Pomeroy (Ed.), Screen Printing. In *Encyclopedia of Materials: Technical Ceramics and Glasses*, Elsevier, Oxford, 2021, pp. 227–232. ISBN 978–0–12-822233-1.

[16] S. Singh, J. Wang, S. Cinti, Review—an overview on recent Progress in screen-printed electroanalytical (bio)sensors, ECS Sens. Plus 1 (2022) 023401, https://doi.org/10.1149/2754-2726/ac70e2.

[17] G. Liang, Z. He, J. Zhen, H. Tian, L. Ai, L. Pan, W. Gong, Development of the screen-printed electrodes: a Mini review on the application for pesticide detection, Environ. Technol. Innov. 28 (2022) 102922, https://doi.org/10.1016/j.eti.2022.102922.

[18] R.D. Crapnell, C.E. Banks, Electroanalytical overview: screen-printed electrochemical sensing platforms, ChemElectroChem 11 (2024) e202400370, https://doi.org/10.1002/celc.202400370.

[19] B. Repič, K. Radan, G. Marolt, A.B. Golob, D. Kuscer, Effect of processing temperature on performance of screen-printed graphite electrodes, Mater. Chem. Phys. (2025) 130455, https://doi.org/10.1016/j.matchemphys.2025.130455.

[20] J.P. Metters, R.O. Kadara, C.E. Banks, Electroanalytical properties of screen printed graphite microband electrodes, Sensors Actuators B Chem. 169 (2012) 136–143, https://doi.org/10.1016/j.snb.2012.04.045.

[21] B.J. Seddon, M.D. Osborne, G. Lagger, R.A.W. Dryfe, U. Loyall, H. Schäfer, H. H. Girault, Micro-glassy carbon inks for thick-film electrodes, Electrochim. Acta 42 (1997) 1883–1894, https://doi.org/10.1016/S0013-4686(96)00401-X.

[22] M. Go, X. Qi, P. Matteini, B. Hwang, S. Lim, High resolution screen-printing of carbon black/carbon nanotube composite for stretchable and wearable strain sensor with controllable sensitivity, Sensors Actuators A Phys. 332 (2021) 113098, https://doi.org/10.1016/j.sna.2021.113098.

[23] L. Liu, Z. Shen, X. Zhang, H. Ma, Highly conductive graphene/carbon black screen printing inks for flexible electronics, J. Colloid Interface Sci. 582 (2021) 12–21, https://doi.org/10.1016/j.jcis.2020.07.106.

[24] A.A. Kava, C. Beardsley, J. Hofstetter, C.S. Henry, Disposable glassy carbon stencil printed electrodes for trace detection of cadmium and Lead, Anal. Chim. Acta 1103 (2020) 58–66, https://doi.org/10.1016/j.aca.2019.12.047.

[25] A.A. Kava, C.S. Henry, Exploring carbon particle type and plasma treatment to improve electrochemical properties of stencil-printed carbon electrodes, Talanta 221 (2021) 121553, https://doi.org/10.1016/j.talanta.2020.121553.

[26] L.M.C. Ferreira, P.S. Silva, K.K.L. Augusto, P.C. Gomes-Júnior, S.O.D. Farra, T. A. Silva, O. Fatibello-Filho, F.C. Vicentini, Using nanostructured carbon black-based electrochemical (bio)sensors for pharmaceutical and biomedical analyses: a comprehensive review, J. Pharm. Biomed. Anal. 221 (2022) 115032, https://doi.org/10.1016/j.jpba.2022.115032.

[27] F.C. Vicentini, T.A. Silva, O. Fatibello-Filho, Carbon black electrodes applied in Electroanalysis, Curr. Opin. Electrochem. 43 (2024) 101415, https://doi.org/10.1016/j.coelec.2023.101415.

[28] J.R. Camargo, L.O. Orzari, D.A.G. Araújo, P.R. De Oliveira, C. Kalinke, D.P. Rocha, A. Luiz Dos Santos, R.M. Takeuchi, R.A.A. Munoz, J.A. Bonacin, et al., Development of conductive inks for electrochemical sensors and biosensors, Microchem. J. 164 (2021) 105998, https://doi.org/10.1016/j.microc.2021.105998.

[29] E. Asadian, M. Ghalkhani, S. Shahrokhian, Electrochemical sensing based on carbon nanoparticles: a review, Sensors Actuators B Chem. 293 (2019) 183–209, https://doi.org/10.1016/j.snb.2019.04.075.

[30] C.C. Villarreal, T. Pham, P. Ramnani, A. Mulchandani, Carbon allotropes as sensors for environmental monitoring, Curr. Opin. Electrochem. 3 (2017) 106–113, https://doi.org/10.1016/j.coelec.2017.07.004.
[31] M.G. Trachioti, A.Ch. Lazanas, M.I. Prodromidis, Shedding light on the calculation of electrode electroactive area and heterogeneous Electron transfer rate constants at graphite screen-printed electrodes, Microchim. Acta 190 (2023) 251, https://doi.org/10.1007/s00604-023-05832-w.
[32] H. Matsuda, Y. Ayabe, Zur Theorie der Randles-Sevčikschen Kathodenstrahl-Polarographie, Z. Für Elektrochem. 59 (1955) 494–503, https://doi.org/10.1002/bbpc.19550590605.
[33] I. Lavagnini, R. Antiochia, F. Magno, An extended method for the practical evaluation of the standard rate constant from cyclic Voltammetric data, Electroanalysis 16 (2004) 505–506, https://doi.org/10.1002/elan.200302851.
[34] S.J. Konopka, Bruce McDuffie, Diffusion coefficients of Ferri- and Ferrocyanide ions in aqueous media, using twin-electrode thin-layer electrochemistry, Anal. Chem. 42 (1970) 1741–1746, https://doi.org/10.1021/ac50160a042.
[35] R.S. Nicholson, Theory and application of cyclic voltammetry for measurement of electrode reaction kinetics, Anal. Chem. 37 (1965) 1351–1355, https://doi.org/10.1021/ac60230a016.
[36] R.O. Kadara, N. Jenkinson, C.E. Banks, Characterisation of commercially available electrochemical sensing platforms, Sensors Actuators B Chem. 138 (2009) 556–562, https://doi.org/10.1016/j.snb.2009.01.044.
[37] K. Jurkiewicz, M. Pawlyta, A. Burian, Structure of carbon materials explored by local transmission Electron microscopy and global powder diffraction probes, C J. Carbon Res. 4 (2018) 68, https://doi.org/10.3390/c4040068.
[38] S.-M. Lee, S.-H. Lee, J.-S. Roh, Analysis of activation process of carbon black based on structural parameters obtained by XRD analysis, Crystals 11 (2021) 153, https://doi.org/10.3390/cryst11020153.
[39] C. Batchelor-McAuley, L.M. Gonçalves, L. Xiong, A.A. Barros, R.G. Compton, Controlling Voltammetric responses by electrode modification; using adsorbed acetone to switch graphite surfaces between adsorptive and diffusive modes, Chem. Commun. 46 (2010) 9037–9039, https://doi.org/10.1039/C0CC03961F.
[40] D. Pamuk, İ.H. Taşdemir, A. Ece, E. Canel, E. Kılıç, Redox pathways of Aliskiren based on experimental and computational approach and its Voltammetric determination, J. Braz. Chem. Soc. (2013), https://doi.org/10.5935/0103-5053.20130162.
[41] M. Dekleva, M. Kovačević, E. Gričar, M. Kolar, B. Genorio, B. Repič, D. Kuščer, H. Prosen, G. Marolt, An innovative pretreatment protocol to eliminate silver contamination-induced Voltammetric interference on graphite-glass working electrode, Electrochem. Commun. 162 (2024) 107707, https://doi.org/10.1016/j.elecom.2024.107707.
[42] M.I. González-Sánchez, B. Gómez-Monedero, J. Agrisuelas, J. Iniesta, E. Valero, Highly activated screen-printed carbon electrodes by electrochemical treatment with hydrogen peroxide, Electrochem. Commun. 91 (2018) 36–40, https://doi.org/10.1016/j.elecom.2018.05.002.
[43] K. Grennan, J.A. Killard, R.M. Smyth, Physical characterizations of a screen-printed electrode for use in an amperometric biosensor system, Electroanalysis 13 (2001) 745–750, https://doi.org/10.1002/1521-4109(200105)13:8/9<745::AID-ELAN745>3.0.CO;2-B.
[44] J. Wang, M. Pedrero, H. Sakslund, O. Hammerich, J. Pingarron, Electrochemical activation of screen-printed carbon strips, Analyst 121 (1996) 345–350, https://doi.org/10.1039/AN9962100345.
[45] M. Šadl, B. Repič, I. Goričan, D. Kuščer, H. Uršič, Aerosol-deposition derived graphite thick films for electrochemical sensors, Inf. MIDEM 54 (2024), https://doi.org/10.33180/InfMIDEM2024.302.
[46] C.K. Chua, Z. Sofer, M. Pumera, Graphite oxides: effects of permanganate and chlorate oxidants on the oxygen composition, Chem. Eur. J. 18 (2012) 13453–13459, https://doi.org/10.1002/chem.201202320.
[47] A.Y.S. Eng, Z. Sofer, P. Šimek, J. Kosina, M. Pumera, Highly hydrogenated graphene through microwave exfoliation of graphite oxide in hydrogen plasma: towards electrochemical applications, Chem. Eur. J. 19 (2013) 15583–15592, https://doi.org/10.1002/chem.201303164.
[48] M. Sýs, E. Khaled, R. Metelka, K. Vytřas, Electrochemical characterisation of novel screen-printed carbon paste electrodes for Voltammetric measurements, J. Serb. Chem. Soc. 82 (2017) 865–877, https://doi.org/10.2298/JSC170207048S.
[49] Glassy carbon disposible electrode - Zensor R&D Available online: https://www.zensorrd.com/GTE100.html (accessed on 7 February 2025).
[50] F. Arduini, A. Amine, C. Majorani, F. Di Giorgio, D. De Felicis, F. Cataldo, D. Moscone, G. Palleschi, High performance electrochemical sensor based on modified screen-printed electrodes with cost-effective dispersion of nanostructured carbon black, Electrochem. Commun. 12 (2010) 346–350, https://doi.org/10.1016/j.elecom.2009.12.028.
[51] F. Arduini, F. Di Nardo, A. Amine, L. Micheli, G. Palleschi, D. Moscone, Carbon black-modified screen-printed electrodes as electroanalytical tools, Electroanalysis 24 (2012) 743–751, https://doi.org/10.1002/elan.201100561.
[52] S. Cinti, F. Arduini, M. Carbone, L. Sansone, I. Cacciotti, D. Moscone, G. Palleschi, Screen-printed electrodes modified with carbon nanomaterials: a comparison among carbon black, Carbon Nanotubes and Graphene, Electroanalysis 27 (2015) 2230–2238, https://doi.org/10.1002/elan.201500168.
[53] P.B. Deroco, O. Fatibello-Filho, F. Arduini, D. Moscone, Effect of different carbon blacks on the simultaneous Electroanalysis of drugs as water contaminants based on screen-printed sensors, Electroanalysis 31 (2019) 2145–2154, https://doi.org/10.1002/elan.201900042.
[54] A. Wong, A.C. Riojas, A.M. Baena-Moncada, M.D.P.T. Sotomayor, A new electrochemical platform based on carbon black paste electrode modified with α-Cyclodextrin and hierarchical porous carbon used for the simultaneous determination of dipyrone and codeine, Microchem. J. 164 (2021) 106032, https://doi.org/10.1016/j.microc.2021.106032.
[55] R. Silva, P. Cervini, R. Martos Buoro, É. Cavalheiro, A new acetylene black and vegetable oil based polyurethane composite: preparation, characterization and its potentialities as an electroanalytical sensor, Mater. Today Commun. 31 (2022) 103691, https://doi.org/10.1016/j.mtcomm.2022.103691.
[56] B. Niemiec, R. Piech, B. Paczosa-Bator, All-solid-state carbon black paste electrodes modified by poly(3-Octylthiophene-2,5-Diyl) and transition metal oxides for determination of nitrate ions, Molecules 28 (2023) 4313, https://doi.org/10.3390/molecules28114313.
[57] M. Hatala, P. Gemeiner, M. Hvojnik, M. Mikula, The effect of the ink composition on the performance of carbon-based conductive screen printing inks, J. Mater. Sci. Mater. Electron. 30 (2019) 1034–1044, https://doi.org/10.1007/s10854-018-0372-7.
[58] J.H.S. Carvalho, J.S. Stefano, L.C. Brazaca, B.C. Janegitz, New conductive ink based on carbon nanotubes and glass varnish for the construction of a disposable electrochemical sensor, J. Electroanal. Chem. 937 (2023) 117428, https://doi.org/10.1016/j.jelechem.2023.117428.
[59] V. Guzsvany, F. Gaál, L. Bjelica, S. Ökrész, Voltammetric determination of Imidacloprid and Thiamethoxam, J. Serbian Chem. Soc. 70 (2005) 735–743, https://doi.org/10.2298/JSC0505735G.
[60] M.B. Brahim, M.F. Elahmadi, H.B. Ammar, Y. Samet, Determination of ultra-trace amounts of neonicotinoid insecticide Imidacloprid by cyclic and square wave Voltammetric methods using pretreated glassy carbon electrode, Glob. NEST J. 20 (2018) 628–636, https://doi.org/10.30955/gnj.002509.
[61] G.-D. Jin, X.-Y. Hu, Study and determination of pesticide Imidacloprid by linear sweep voltammetry at a Prussian blue and MWNT modified glassy carbon electrode, Chin. J. Anal. Lab. 27 (2008) 14.
[62] J. Liu, Y. Li, G. Song, K. Zhang, B. Ye, Sensitive determination of pesticide Imidacloprid using a glassy carbon electrode modified with a film composed of multi-walled carbon nanotubes and poly(aspartic acid), Int. J. Environ. Anal. Chem. 94 (2014) 884–900, https://doi.org/10.1080/03067319.2014.914182.
[63] M. Zhang, H.T. Zhao, X. Yang, A.J. Dong, H. Zhang, J. Wang, G.Y. Liu, X.C. Zhai, A simple and sensitive electrochemical sensor for new neonicotinoid insecticide Paichongding in grain samples based on β-Cyclodextrin-graphene modified glassy carbon electrode, Sensors Actuators B Chem. 229 (2016) 190–199, https://doi.org/10.1016/j.snb.2016.01.119.
[64] Y. Zhao, X. Zheng, Q. Wang, T. Zhe, Y. Bai, T. Bu, M. Zhang, L. Wang, Electrochemical behavior of reduced graphene oxide/Cyclodextrins sensors for ultrasensitive detection of Imidacloprid in Brown Rice, Food Chem. 333 (2020) 127495, https://doi.org/10.1016/j.foodchem.2020.127495.
[65] Q. Wang, H. Zhangsun, Y. Zhao, Y. Zhuang, Z. Xu, T. Bu, R. Li, L. Wang, Macro-Meso-microporous carbon composite derived from hydrophilic metal-organic framework as high-performance electrochemical sensor for neonicotinoid determination, J. Hazard. Mater. 411 (2021) 125122, https://doi.org/10.1016/j.jhazmat.2021.125122.
[66] B.E. Castillo, E. Prokhorov, G. Luna-Bárcenas, Y. Kovalenko, Potential use of chitosan-TiO_2 nanocomposites for the electroanalytical detection of Imidacloprid, Polymers 14 (2022) 1686, https://doi.org/10.3390/polym14091686.